

## IRACON PROPAGATION MEASUREMENTS AND CHANNEL MODELS FOR 5G AND BEYOND

Sana Salous<sup>1</sup>, Fredrik Tufvesson<sup>2</sup>, Kenan Turbic<sup>3</sup>, Luis M. Correia<sup>3</sup>, Thomas Kürner<sup>4</sup>, Diego Dupleich<sup>5</sup>, Christian Schneider<sup>5</sup>, Daniel Czaniera<sup>5</sup>, Belen Montenegro Villaceros<sup>6</sup>

<sup>1</sup>Durham University, UK, <sup>2</sup>Lund University, Sweden, <sup>3</sup>IST/INESC-ID-University of Lisbon, Portugal, <sup>4</sup>Technische Universität Braunschweig, Germany, <sup>5</sup>Technische Universität Ilmenau, Germany, <sup>6</sup>European Commission Joint Research Centre, Italy

**Abstract** – Several frequency bands and system architectures are proposed for 5G and beyond to meet the higher data rates for point-to-point communication and point-to-area coverage. In this paper, we present radio propagation studies and models developed in typical scenarios for massive antenna deployment and body area networks, in frequency bands below 6 GHz, building entry loss and clutter loss and vehicular communication, in the millimeter wave bands, and models in the Terahertz for 5G and beyond.

**Keywords** – Body Area Network, Building Entry Loss, Channel Model, Clutter Loss, COST IRACON, Massive MIMO, mm Wave, Terahertz, Vehicle to Vehicle

### 1. INTRODUCTION

The European Cooperation in Science and Technology, (COST) action on inclusive radiocommunication networks for 5G and beyond (IRACON) aims to develop more accurate radio channel models for inclusive deployment scenarios. The particulars of millimeter wave propagation in various frequency bands identified by the World Radiocommunication Conference in 2015 (WRC15) and massive multiple-input multiple-output (MIMO) channels below 6 GHz are of immense interest to achieve the anticipated higher data rates for future radio networks.

Several research groups developed custom-designed radio channel sounders, and performed measurements to develop suitable models. In this paper, radio propagation measurements and models developed within the COST IRACON action are presented. These include body area networks (BAN), indoor and outdoor massive MIMO below 6 GHz, vehicle-to-vehicle channels for millimeter wave and below 6 GHz, millimeter wave clutter loss (CL), building entry loss (BEL) and terahertz (THz) communication.

### 2. BODY AREA NETWORK CHANNEL MODELS

In BAN communication scenarios, data are exchanged with devices inside the human body, on it, or in its close surroundings as in Fig. 1. One distinguishes in, on, off and into-body channels, considering whether communication takes place

inside the body, along its surface, involving an external access point (AP), or traversing the boundary between in and outside the body.

The COST IRACON empirical off-body channel model is composed of a log-distance mean path loss (MPL) and two fading components, as given in (1).

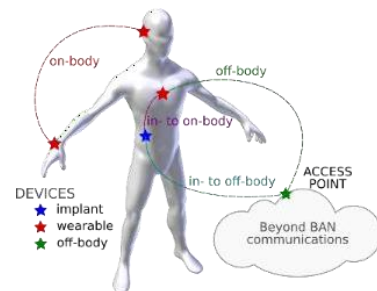


**Fig. 1** – BAN configurations

$$L_{pl[\text{dB}]} = L_0(d_0) + 10n_{pl} \log(d/d_0) + \Delta L_{ls} + \Delta L_{ss} \quad (1)$$

where  $d$  is the distance between the transmitter (Tx) and receiver (Rx),  $L_0(d_0)$  is the MPL at the reference distance  $d_0$  (usually 1 m),  $n_{pl}$  is the path-loss exponent,  $\Delta L_{ls}$  and  $\Delta L_{ss}$  are the large and small-scale fading components, represented by independent random variables. Large-scale fading exhibits a log-normal distribution, whereas small-scale fading distributions include Rice, Nakagami-m, Rayleigh and log-normal distributions. Model parameters at 2.45 GHz, obtained from several measurements are summarized in Table 1, where  $\mu_{Ln[\text{dB}]}$  (log-mean) and  $\sigma_{Ln[\text{dB}]}$  (log-standard deviation) are the parameters for the log-normal distribution, and  $m_{Nk}$  (shape) and  $\Omega_{Nk}$  (scale) are the Nakagami

distribution parameters. For off-body propagation, due to the inability to de-embed the antennas' radiation patterns from measurements, the measured loss corresponds to the system loss. The model parameters represent a typical indoor office environment [1-2], for static, quasi-dynamic (mimicking walk in a given position) and dynamic user scenarios (approaching and departing from the AP), with both co- [2] and cross-polarized antennas [1]. The table also gives the model parameters for measurements inside a dome-shaped discotheque within a ferry, with the user walking towards and away from a fixed AP [3].

**Table 1** – Summary of MPL and fading parameters for the off-body channel at 2.45 GHz

Env.	Mean path loss		Large-scale fading		Small-scale fading	
	$L_0(d_0)$ [dB]	$n_{pl}$	$\mu Ln$ [dB]	$\sigma Ln$ [dB]	$m_{Nk} \in$	$\Omega_{Nk} \in$
Office	32.0-50.0	1.71	0	1.2-3.0	0.9-19.5	1.0-2.0
Ferry	25.2-64.7	1.69	0	1.7-6.5	0.8-1.5	1.5-2.1

Two variants of the MPL model are proposed for in and into-body channels: a log-distance model (2) and a linear model (3), i.e.

$$L_{pl[dB]} = L_{0,\alpha}(d_0) + 10\alpha_{pl} \log(d/d_0) \quad (2)$$

$$L_{pl[dB]} = L_{0,\beta}(d_0) + 10\beta_{pl}[dB/cm]d_{[cm]} \quad (3)$$

where  $d$  is the Tx-Rx distance,  $L_{0,\alpha/\beta}(d_0)$  is the MPL at the reference distance  $d_0$  usually taken at 1 cm, and  $\alpha_{pl}$  and  $\beta_{pl}$  are slopes of the MPL models.

The in-body channel corresponds to links established between two implants (in2in). Into-body covers implants, e.g. an ingested capsule streaming video to a receiver placed on the patient's body (in2on) or off-body next to it (in2off). Table 2 summarizes the model parameters for two channels: between two implants (in2in) and in to off-body (in2off), and for in to on-body (in2on) for the 3.1 - 5 GHz band. The path-loss standard deviation around the MPL ( $\sigma$ ), and applicable distances ( $d$ ) are also provided.

**Table 2** – Summary of the MPL model parameters for in2in, in2on, and in2off-body channels at 3.1-8.5 GHz

Ch.	$L_{0,\alpha}(d_0)$ dB	$\alpha_{pl}$	$L_{0,\beta}(d_0)$ dB	$\beta_{pl}$ dB/cm	$\sigma$ dB	$d$ cm
in2in	-	-	45	4.6	4.3	3-8
in2off	70.4-71.5	0.7-1.4	-	-	-	4-50
in2on	-12.2-35.8	5.8-9.3	14.8-53.4	4.5-7.4	5-5.7	2.8-8

The parameters were derived from full-wave numerical simulations, and from wideband measurements using physical liquid phantoms with one antenna fixed at 3.5 cm from the phantom's surface while the other was moved in the air over a spatial grid [4], or in vivo. The in to off-body channel was parameterized based on in vivo and phantom-based measurements [5].

### 3. MASSIVE MIMO BELOW 6 GHz

The COST 2100 MIMO channel model [6] is a spatially consistent geometry based stochastic channel model (GSCM) that uses the concepts of clusters and visibility regions. In COST IRACON the extension of the model to massive MIMO channels [7] includes: 1) introduction of the visibility regions at the base station, 2) introduction of a gain function of individual multipath components MPCs, and 3) generalization to full 3D geometries. A MATLAB implementation is freely available [8].

The visibility regions at the base station is motivated by the fact that when the antenna array gets physically larger, the radio channel cannot be seen as wide-sense stationary (WSS) over the array, clusters appear and disappear, which means that both the angular spread and the delay spread change over the array. This effect is not captured by conventional MIMO channel models.

Measurements in [9] indicate that individual multipath components (MPCs) have a limited lifetime within the cluster when the user equipment moves with different MPCs of a cluster active at different locations within a visibility region. This is modeled by a gain function, with a Gaussian shape in the spatial domain with its peak randomly located within the cluster for each MPC. These gain functions act as weighting functions for the MPCs so that depending on where the user equipment is located in the visibility region it sees different weighted combinations. This retains the spatial consistency of the model, which is also important when the model is used for more advanced forms of radio-based localization and navigation.

The generalization to 3D geometries and support of polarimetric channels allow for advanced antenna arrangements to be used for massive MIMO. The base stations, individual antenna locations, user equipment, scatterer locations, and visibility regions can all be described by their 3D coordinates. Antenna gain patterns are included for each antenna. The COST family of channel models inherently captures spherical wave front effects as

scatterer locations are defined by their coordinates in the simulation area rather than their directions with respect to the base station and user equipment antennas. As the model output is the transfer function matrix between the base station antenna array and the antennas of the user equipment, any kind of digital, hybrid or analog beamforming is supported.

**Massive MIMO extensions:** Visibility regions are used at the base station to model the appearance and disappearance of clusters along a physically large array as a death-birth process along the array. The appearance/disappearance of new clusters are modeled by a Poisson process along the array with intensity  $\lambda$  new clusters per meter. The number of observed base station visibility regions for an array spanning the interval  $x_1$  to  $x_2$  is given by (4):

$$N(x_1, x_2) \in P_0\{\lambda(x_2 - x_1) + \lambda E(Y)\} \quad (4)$$

where  $E(Y)$  is the scenario dependent mean length of the visibility area at the base station [7]. Fig. 2 shows a measurement example with a 7.5 m uniform linear array in a line-of-sight (LOS) scenario at 2.6 GHz. Over the the whole array the median value of clusters is 23, but not all of them are visible at the same spot of the array. Six clusters can (in the median) be seen over the whole array, and 17 clusters at some parts.

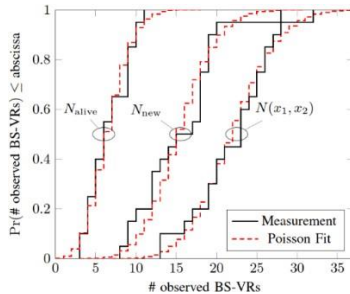


**Fig. 2** – Visibility regions over a large array.  $N(x_1, x_2)$  is the number of observed visibility regions (or clusters),  $N_{new}$  is the number of appearing visibility regions and  $N_{alive}$  is the number of already existing visibility regions.

The gain function describes the appearance and disappearance of individual multipath components. The lifetime, or the length of the spatial region within the visibility region where a MPC has a significant contribution, is a random parameter determining the radius of the MPC visibility region and the corresponding width of the gain function. Fig. 3 shows an example of MPC lifetime from a LOS measurement in an indoor sports hall [9]. Many of the MPCs have relatively short lifetimes with a few MPCs observed over the whole route of the user. These sports hall measurements show that MPC

lifetimes are best described by a log-normal distribution for the radii of the MPC visibility regions. For a smooth onset of the activation of a specific MPC the relative contribution of each MPC is modeled by a gain function, with a Gaussian profile as in (4) which multiplies the complex amplitude of each MPC. Thus, the weight of a particular MPC depends on the Euclidean distance between the user equipment position  $r_{MS}$  and the center of the  $l$ -th MPC visibility.

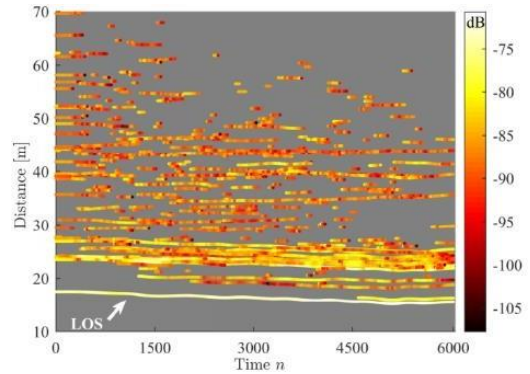


**Fig. 3** – The distance on the y-axis is the propagation distance for the MPCs, whereas the time on the x-axis indicates the different channel snapshots.

The lifetime of the MPC, determined by the width of the Gaussian profile, is controlled by  $\sigma_{g,l}$  and is modeled as a log-normal parameter as in (5) [7].

$$g_{MPC,l}(r_{MS}) = \exp(-d(r_{MS} - r_g)^2 / 2\sigma_{g,l}^2) \quad (5)$$

The COST IRACON massive MIMO extension is parameterized and validated based on measurements for physically large outdoor arrays at 2.6 GHz in LOS and non-LOS (NLOS), and with indoor and outdoor measurements for closely located users at 2.6 GHz. A detailed model description can be found in [7].

## 4. VEHICLE TO VEHICLE

In this section, we analyze the radio channel for vehicle-to-vehicle (V2V) communication from the sub-6 GHz to the mm-wave band. We investigate the challenging cases of propagation characteristics in a transition from LOS to NLOS in a corner scenario and an urban crossroad.

### 4.1 Corner scenario at mm-waves

Here we focus on the effect of the transition from LOS to NLOS in a corner scenario. Simultaneous measurements at 30 GHz, 60 GHz and 6.75 GHz were conducted using the multiband approach in [10]. To emulate the transition of (V2V) communication from LOS to obstructed line of sight

(OLOS) to NLOS when the Rx turns around the corner, the Tx was fixed, while the Rx was moved to different locations as in Fig. 4. The antennas were placed at a typical height of a vehicle at 1.55 m and both the Tx and Rx antennas with 30° HPBW were rotated with 30° to scan the complete azimuth domain at 0° elevation to synthesize the omnidirectional power delay profile (PDP), as in Fig. 5. Five Rx positions were measured to show the transition from LOS to being obstructed by the vegetation in the corner and then being blocked by Building B. Position 1 was measured twice: Position 1a without parked vehicles in the scenario (blue bullets), and Position 1b with parked vehicles in the surrounding area. The resulting total link budget is shown in Fig. 6, where there is a total maximum loss (path loss plus obstruction loss) of approximately 17 dB at 60 GHz.

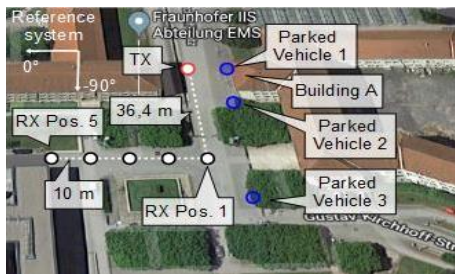


Fig. 4 – Measurement set-up in the corner scenario

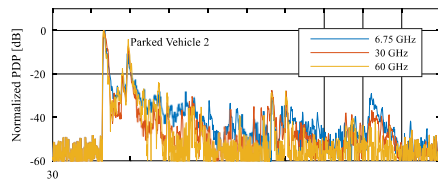


Fig. 5 – Synthetic omnidirectional PDP for position 1b

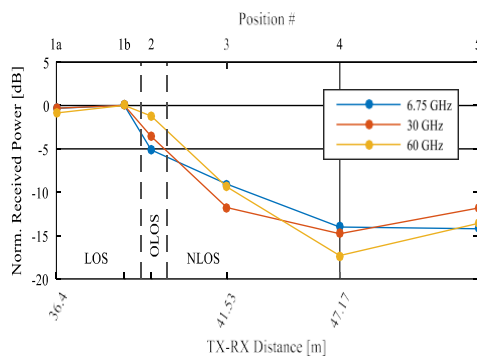


Fig. 6 – Received power vs Tx-RX distance

## 4.2 Urban intersections

To develop next generation wireless systems for vehicles, detailed propagation models are needed. Particularly, there is a need for a spatially consistent model that can reflect the non-stationarities of the vehicular channel and that can support multi-antenna configurations at both ends, either for beamforming purposes, or for spatial multiplexing, or just for diversity. Previously, member institutions of the COST 2100 and IC1004 actions have derived a GSCM for V2V communication in highway scenarios and a non-stationary model for vehicular communication, but a detailed measurement-based propagation model supporting multiple antenna configurations with realistic spatio-temporal characteristics in urban intersections has been lacking until now.

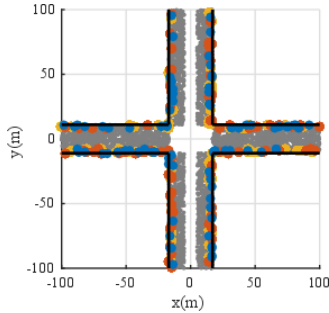
The COST IRACON channel model for urban intersections [11] is a GSCM based on a street geometry defined by a map. It can thus represent typical intersection scenarios or specific intersections. Specular scatterers are randomly dropped, with a given density (number of specular scatterers per unit area), in the simulation area in bands along the walls according to the geometry of the intersection. These scatterers are then labeled as first, second and third order reflection points. Similarly, diffuse scatterers are also randomly placed along with the walls, but in wider bands. For simulations of specific intersections, especially for simulations of wider or more open intersections, scatterers can also be dropped in areas that are not aligned with the walls. These scatterers typically represent contributions from lamp posts or larger street signs, which typically can be observed in measurements. Table 3 summarizes the intensity,  $\chi$ , of different types of scatterers as well as the width,  $W$ , of the bands of scatterers along the walls.

Table 3 – Intensity and width of the bands for random scatterer drop for the different types of MPCs

Type	Order	$\chi$ (m <sup>-2</sup> )	$W$ (m)
Wall	1st	0.044	3
Wall	2nd	0.044	3
Wall	3rd	0.044	3
Non-wall	1st	0.034	User defined
Diffuse, wall	1st	0.61	12
Diffuse, non-wall	1st	0.61	User defined



Fig. 7 shows an example of a drop of scatterers from a real intersection in Berlin, Germany. Here, the blue, red, yellow and gray dots represent first-, second-, third-order and diffuse scatterers, respectively.



**Fig. 7** – Example of scatterers dropped in a simulation area. Colored dots are specular components, grey dots represent diffuse scattering.

Once the scatterers are dropped in the simulation area the contribution of each scatterer to the impulse response is determined by expressions for: 1) distance dependence, 2) losses due to interactions with scattering objects, 3) obstructions by buildings, foliage and other objects, 4) diffraction around corners, 5) angular dependence of the scattering interaction, and 6) random, but spatially correlated, large-scale fading.

The transfer function of the channel between any two antennas are calculated as a superposition of all power weighted contributions from the scatterers as in (6):

$$H(f, t) = \sum_{l=1}^L g_l e^{-j2\pi f \tau_l} G_{Tx}(\Omega_{Tx}) G_{Rx}(\Omega_{Rx}) \quad (6)$$

where  $G$  is the complex antenna amplitude gain in direction  $\Omega$ ,  $g_l$  is the complex amplitude of path  $l$ ,  $L$  is the total number of paths,  $f$  is the frequency, and  $\tau_l$  is the propagation delay,  $\tau_l = d_l/c$ . For each MPC the average path power gain is modeled as in (7):

$$\bar{g}(d)^2 = \left( \frac{g_0 g_a g_b}{d} \right)^2 10^{-L_p/10} \quad (7)$$

where  $d$  is the path propagation distance and  $g_0^2$  is the path power gain at a reference distance of 1 m. The term  $g_a^2$  describes the path angular power gain, which is a function of the incoming and outgoing angles for each scatterer, and  $g_b^2$  is a gain describing the effects of obstruction and blockage by buildings. Each multipath component then undergoes spatially correlated Gamma distributed large-scale fading (with parameters  $k$  and  $\theta$ ) so that the instantaneous amplitude of each MPC varies around the mean according to a Nakagami distribution. The autocorrelation of the fading process is described by a conventional Gudmundson model [12] with

coherence distance  $d_c$ . Table 4 summarizes the path gain parameters for the different contributions, where  $G_0 = 20 \log_{10}(g_0)$ .

The model was parameterized and verified against measurements in various types of street intersections in Berlin, Germany. Fig. 8 shows an example of simulated and measured impulse responses from the intersection outlined in Fig. 7. The y-axis shows the measurement time and the x-axis shows the propagation distance of the multipath components. The measurements are performed with an ultra-wideband channel sounder at a center frequency of 5.7 GHz with a bandwidth of 1 GHz. The white stripes in the left plot are due to the data storage process where no measurements could be taken.

As seen in the figure there is a very good correspondence between the outputs of the channel model and the real-life measurements. Some detailed behavior differs, but the overall structure of the channel evolution and variation of the impulse response is well captured by the GSCM.

**Table 4** – Path gain parameters for the different multipath contributions

Type	Order	$G_0$ (dB)	$d_c$ (m)	$k$ (-)	$\theta$ (-)
Wall	1st	U(-65, -48)	U(1, 2)	U(2, 8)	1/k
Wall	2nd	U(-70, -59)	U(0, 1.5)	U(1, 6)	1/k
Wall	3rd	U(-75, -65)	U(0, 1)	U(1, 4)	1/k
Non-wall	1st	U(-68, -52)	U(0, 1)	U(1, 6)	1/k
Diff.	1st	U(-80, -68)	U(0, 1)	U(1, 1)	1/k

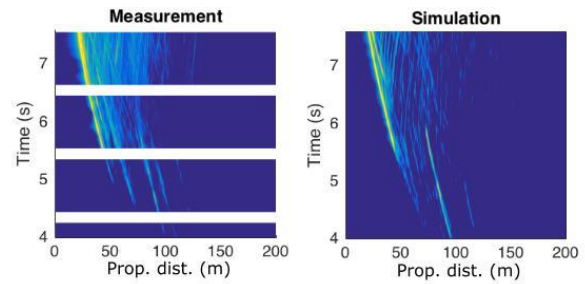


**Fig. 8** – Measured and simulated impulse responses over time in the intersection in Fig. 7. The white stripes are due to data download, with no measurements.

## 5. BUILDING ENTRY LOSS AND CLUTTER LOSS AT 26 GHz

Currently there are two separate ITU-R P-series Recommendations on building entry loss (BEL), ITU-R P.2109-0 and clutter loss (CL) ITU-R P.2108-0. In sharing studies, BEL and CL are treated as multiplicative where the overall excess path loss is the sum in dB of the individual losses. To assess

this approach, separate BEL and CL measurements were performed using the multiband, wideband channel sounder of Durham University operating between 25.5-28.5 GHz [13], at JRC site in Ispra, Italy, and the results compared with combined CL and BEL measurements. The site has 2 or 3 story buildings having an average building height of 12 m, parking zones, green areas, squares and office centers. The transmitter was mounted on a cherry picker at 25 m height in location *Tx1* for clutter loss and combined CL and BEL. For BEL measurements, it was mounted at 7 m height in location *Tx2* (Fig. 9). The receiver was placed on a trolley at 1.5 m height above ground level for all measurement scenarios.

For CL, data were collected outside the building as indicated by the route RX OUT every 1 m, and then inside the building for combined CL and BEL, in offices and in the corridors closest to the illuminated façade of the building. For BEL, measurements were taken outside the building and inside the building for *Tx2* position. In all scenarios, the equivalent isotropic radiated power (*EIRP*) was 48 dBm and the antenna beam width was 20°. The receive antenna was omnidirectional in all the measurements except for the combined clutter and building entry loss measurements. Fig.10 shows examples of PDPs collected in the clutter scenario. Accurate position information with centimeter-level accuracy was obtained using a total station (Leica PTS1200) and GNSS data. The PDPs were used to estimate the received power, and then to estimate BEL and CL according to ITU recommended procedures.

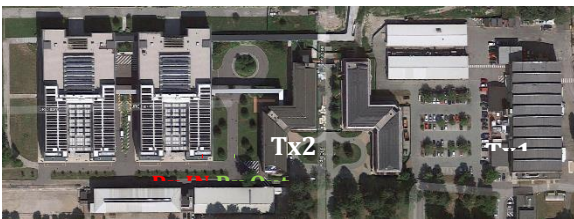


Fig. 9 – Measurement scenario

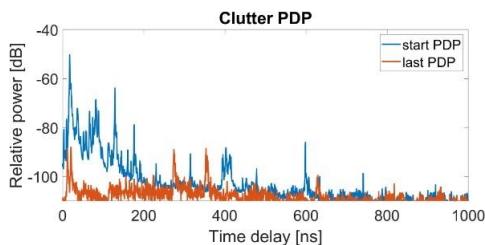


Fig. 10 – PDP in clutter

Fig. 11 shows the CDF for BEL from *Tx1* and *Tx2*, with median values equal to 44.03 dB and 45.8 dB. The results show that the difference in the median value of BEL between the two methods is ~1.8 dB, which indicates that either method can be used for estimating the median value of BEL. BEL exhibited higher loss than clutter loss above the median value due to measurements taken on the higher floors. The CDF of the clutter loss was also estimated with a median loss value of 18 dB.

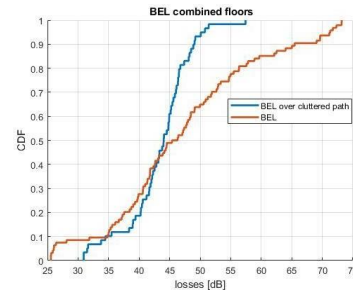


Fig. 11 – CDF of BEL from *Tx1* and *Tx2*

## 6. CHANNEL MODELING FOR THz COMMUNICATION

Wireless communication in the lower THz frequency band from around 300 GHz has become of interest for the community in the last couple of years with the realization of several hardware demonstrations, leading into the development of the first IEEE standard [14]. At WRC 2019 the frequency range 275-450 GHz and its usage for THz communication is subject to agenda item 1.15. From the propagation point of view in this frequency range a couple of phenomena are different from those at the lower frequency bands. Therefore, we focus on these effects and phenomena taking the following three environments into account and provide a short description of the state of the art: atmospheric effects for outdoor scenarios, the specific effects of scattering and reflections in indoor environments and the specific phenomena for close proximity communication.

### 6.1 Atmospheric effects for outdoor applications

At 300 GHz and beyond atmospheric effects play a major role especially if the distance between the transmitter and receiver exceeds a few meters. In this case three relevant propagation mechanisms are contributing [15]: atmospheric gas attenuation, cloud and fog attenuation, and rain attenuation. The overall path loss at a distance  $d$  and a carrier frequency  $f$  can be modeled as in (8):

$$L_{[dB]} = 92.4 + 20 \log(d_{[km]}) + 20 \log(f_{[GHz]}) + (\gamma_0 + \gamma_w + \gamma_R + \gamma_c)d_{[km]} \quad (8)$$

where,  $\gamma_0$ : represents specific attenuation due to dry air,  $\gamma_w$ : specific attenuation due to water vapour,  $\gamma_R$ : specific attenuation due to rain, and  $\gamma_c$ : specific attenuation due to fog and clouds.

Methods for the calculation of specific attenuations can be found in three ITU-R Recommendations: ITU-R P.676-11 on attenuation by atmospheric gases and related effects, ITU-R P.838-3 on specific attenuation model for rain for use in prediction methods and ITU-R P.840-6 on measurements of ionospheric and related characteristics. Exemplary results of the total specific attenuation at 300 GHz for different regions in the world with various weather conditions [15-16] are presented in Table 5 using (8) and the ITU-R Recommendations. Ray-optical modeling in indoor environments

For propagation modeling in indoor environments at THz frequencies ray-optical approaches show reasonably good agreement with channel measurements [17]. While such ray-optical approaches are known from lower frequencies, the electromagnetic modeling of the scattering and reflection processes is different at THz frequencies due to the small wavelength, which becomes less than 1 mm at carrier frequencies beyond 300 GHz. Therefore, structures on the order of a wavelength have to be taken into account. These include: (1) diffuse scattering off the specular direction from walls and objects with a surface roughness of less than 1 mm (i.e. standard deviation of the height variation). This was shown by THz time-domain spectroscopy and simulations using modified reflections coefficients [18]. Although the diffuse scattering field may be weak in comparison to the specular direction, it is still high enough to enable NLOS links over short distances; (2) layered media with layer thickness on the order of a wavelength may cause multiple reflections causing destructive interference if the reflected waves are at discrete scattering angles [19]. Recent channel sounder measurements in a real data center at 300 GHz [20] with a great deal of highly reflective materials have shown, that despite the high path loss significant multipath propagation can be observed.

**Table 5** – Total specific attenuation in dB/km at 300 GHz

Description in [14, 15, 16].	Atten. dB/km
Bangkok, temp. 35°C, relative humidity 90%, no rain	32.1
Bangkok, temp. 35°C, relative humidity 90%, , rain (50 mm/h)	51.1
Basra, temp. 43°C, relative humidity 30%, dust (10 m visibility)	27.8
Berkeley, temp. 20°C, relative humidity 60%, fog (100m visibility)	9.5
Bellingham, temp. 22°C, relative humidity 50%, rain (4mm/h)	10.5
Boulder, temp. 20°C, relative humidity 44%	5.8
Buffalo, temp. -10°C, relative humidity 30%	0.4
Boulder, with clouds (100m of large cumulus clouds), temp. 20°C, relative humidity 44%	44.7

## 6.2 Models for close-proximity communications.

The transmission with ultra-high data rates of very short distances, the so-called close-proximity communication, has recently drawn some attraction involving propagation phenomena, which are specific to such environments: (1) in the so-called kiosk downloading applications multiple bouncing signals between the metallic parts of the set-up are causing a high degree of inter-symbol interference which needs to be taken into account in link-level simulations for the design and standardization of new systems. For these simulations, typically stochastic channel models are applied [21]; (2) in intra-device applications wireless transmission is realized for example between mother boards of computers or between a sensor and a memory card inside a camera. In these cases the modeling of reflection and scattering processes in metallic enclosures [22] and at printed circuit boards (PCB) are of interest [23]

## 7. CONCLUSION

In this paper, propagation models and measurements for typical environments for 5G and beyond have been presented. Below 6 GHz frequency bands have been investigated for massive MIMO and vehicular propagation, extending the COST 2100 model to cover these new applications. Vehicular communication in a corner scenario and a crossroad below 6 GHz and in the millimeter wave bands have been modeled from measurements and simulations. Path-loss models for body area networks for short-range in-body and in-body-to-off-body scenarios, as well as in office and ferry environments are discussed. The impact

of clutter and building entry loss on millimeter wave propagation have been presented from measurements at 26 GHz and the method proposed by ITU-R Recommendations for combining the two losses was confirmed for the median value of building entry loss. THz propagation typical loss parameters are given. Although these high frequency bands are currently considered for short-range applications such as data centers, recently they have been proposed for car-to-X communications and in intelligent transportation systems where in railway environments various different propagation scenarios have been already identified for smart rail applications.

## ACKNOWLEDGEMENT

The authors acknowledge the fruitful discussions in COST Action CA15104 IRACON. The authors would also like to thank all the contributors to the research in the different institutions.

## REFERENCES

- [1] K. Turbic, S. J. Ambroziak, and L. M. Correia, "Characteristics of the Polarised Off-Body Channel in Indoor Environments," *EURASIP J. Wireless Commun. Netw.*, vol. 2017, no. 1, p. 174, Oct. 2017.
- [2] S. J. Ambroziak, L. M. Correia, R. J. Katulski, M. Mackowiak, C. Oliveira, J. Sadowski, and K. Turbic, "An Off-Body Channel Model for Body Area Networks in Indoor Environments," *IEEE Trans. Antennas Propag.*, vol. 64, no. 9, pp. 4022–4035, Sep. 2016.
- [3] P. T. Kosz, S. J. Ambroziak, J. Stefanski, K. K. Cwalina, L. M. Correia, and K. Turbic, "An Empirical System Loss Model for Body Area Networks in a Passenger Ferry Environment," in *Proc. URSI'18 - Baltic URSI Symposium*, Poznan, Poland, May 2018.
- [4] C. Andreu, C. Garcia-Pardo, A. Fornes-Leal, N. Cardona, S. Castello-Palacios, and A. Valles-Lluch, "Spatial In-Body Channel Characterization Using an Accurate UWB Phantom," *IEEE Trans. on Microwave Theory and Techniques*, vol. 64, no. 11, pp. 3995-4002, Nov. 2016.
- [5] C. Garcia-Pardo, A. Fornes-Leal, C. Andreu, N. Cardona, S. Castello-Palacios, A. Valles-Lluch, R. Chavez-Santiago, and I. Balasingham, "Experimental Ultra Wideband Path Loss Models for Implant Communications," *PIMRC'16*, Valencia, Spain, Sep. 2016.
- [6] L. Liu et al., "The COST 2100 MIMO channel model," in *IEEE Wireless Commun.*, vol. 19, no. 6, pp. 92-99, Dec. 2012.
- [7] J. Flordelis, X. Li, O. Edfors, F. Tufvesson, "Massive MIMO Extensions to the COST 2100 Channel Model: Modeling and Validation", *IEEE Trans. Wireless Commun.*, *Under review*. <https://arxiv.org/abs/1905.04931>
- [8] "COST 2100 channel model, public domain implementation," available: <https://github.com/cost2100>.
- [9] X. Li, E. Leitinger et al., "Massive MIMO-based localization and mapping exploiting phase information of multipath components," *IEEE Trans. Wireless Commun.*, 2019.
- [10] D. Dupleich et al., "Multi-band Characterization of Path-loss, Delay, and Angular Spread in V2V Links," *Proc. PIMRC 2018*, Bologna, Italy, Sep. 2018.
- [11] C. Gustafson, K. Mahler, D. Bolin, F. Tufvesson, "The COST IRACON Geometry-based Stochastic Channel Model for Vehicle-to-Vehicle Communication in Intersections", *IEEE Trans. on Vehicular Technology*, *Under review*. <http://arxiv.org/abs/1903.04788>
- [12] M. Gudmundson, "Correlation model for shadow fading in mobile radio systems," *Electron. Lett.*, vol. 27, no. 23, pp. 2145-2146, 7 Nov. 1991.
- [13] X. Raimundo, S. El-Faitori, and S. Salous, "Multi-band outdoor measurements in a residential environment for 5G networks," *EUCAP'18*, London, UK, Apr. 2018.
- [14] IEEE Std for High Data Rate Wireless Multi-Media Networks-Amendment 2: 100 Gb/s Wireless Switched Point-to-Point Physical Layer," *IEEE Std 802.15.3d-2017*, vol., no., pp. 1-55, Oct. 2017
- [15] Channel Modeling Document (CMD)," <https://mentor.ieee.org/802.15/dcn/14/15-14-0310-18-003d-channel-modeling-document.docx>.



- [16] H2020 ThoR Deliverable D2.2; Overall System Design, [www.thorproject.eu](http://www.thorproject.eu)
- [17] S. Priebe, M. Kannicht, M. Jacob and T. Kürner, "Ultra Broadband Indoor Channel Measurements and Calibrated Ray Tracing Propagation Modeling at THz Frequencies," *J. Commun. and Netw.*, Vol. 15, No. 6, pp. 547-558, Dec. 2013.
- [18] C. Jansen, S. Priebe, C. Möller, M. Jacob, H. Dierke, M. Koch, T. Kürner, "Diffuse Scattering from Rough Surfaces in THz Communication Channels". *IEEE Trans. THz Sci. Technol.*, Vol. 1, No. 2, pp. 462-472, 2011.
- [19] J. Kokkonen, V. Petrov, D. Moltchanov, J. Lehtomaeki, Y. Koucheryavy and M. Juntti, "Wideband Terahertz Band Reflection and Diffuse Scattering Measurements for Beyond 5G Indoor Wireless Networks," *Proc. EW'16*, Oulu, Finland, May 2016.
- [20] J. Eckhardt, T. Doeker, S. Rey, T. Kürner, "Measurements in a Real Data Centre at 300 GHz and Recent Results", *Proc. EuCAP'19*, Krakow, Poland, Apr. 2019
- [21] D. He, K. Guan, et al., "Stochastic Channel Modeling for Kiosk Applications in the Terahertz Band". *IEEE Trans. THz Sci. Technol.*, Vol. 7, No. 5, pp. 502-513, 2017.
- [22] A. Zajic and P. Juyal, "Modeling of THz chip-to-chip wireless channels in metal enclosures," *Proc. EuCAP'18*, London, UK, Apr. 2018.
- [23] A. Fricke, M. Achir, P. Le Bars, T. Kürner, "A Model for the Reflection of Terahertz Signals from Printed Circuit Board Surfaces", *Int. J. Microw. Wireless Technol.*, Vol. 10, No. 2, pp. 179-186, Mar. 2018.